# Development of the Cube Component $(\{001\}\langle100\rangle)$ During Plane Strain Compression of Copper and Its Importance in Recrystallization Nucleation



SUPRIYO CHAKRABORTY, CHAITALI S. PATIL, and STEPHEN R. NIEZGODA

The origin of cube texture during recrystallization of medium to high stacking-fault energy FCC metals has been debated for several decades. However, the evolution of cube component during deformation is not studied well and hence, it is still unclear what are the favorable nucleation sites for the cube oriented recrystallized grains. To resolve this issue, we applied a full field crystal plasticity model utilizing a dislocation density based constitutive theory for the simulation of plane strain compression of polycrystalline copper. Simulation results reveal that the grains with initially cube orientation retained a small fraction of the cube component in the deformed state, whereas, some of the grains with initially non-cube orientations developed the cube component during the deformation. For strain up to 0.46, non-cube grains which are within 10 to 20 deg from the ideal cube orientation showed the highest tendency to develop the cube component during deformation. However, the cube component developed during the deformation was unstable and rotated away from the cube orientation with further deformation. With increasing strain up to 1.38, some of the grains with higher angular deviation from the ideal cube orientation also developed the cube component. No particular axis preference was observed for the non-cube grains, rather, the evolution of the cube component becomes dynamic at larger strain. Analysis of the disorientation angle and the dislocation density difference with the neighboring locations shows that the cube component developed during the deformation can play a significant role during nucleation. These findings will be useful for controlling the cube texture in FCC metals.

https://doi.org/10.1007/s11661-021-06513-0 © The Minerals, Metals & Materials Society and ASM International 2021

## I. INTRODUCTION

CRYSTALLOGRAPHIC texture plays an important role in wide range of engineering applications. For example, a sharp texture (either the rolling texture or the cube texture) in aluminum and aluminum alloys lead to plastic anisotropy which causes 'earing' or wavy top during deep drawing processes. Therefore, a mixed texture is desirable to maintain uniform material flow during the deep drawing process. [1-3] On the other hand, nickel or copper substrates with strong cube textures are favored for epitaxial growth of high temperature superconductors. [4-6]

SUPRIYO CHAKRABORTY and CHAITALI S. PATIL are with the Department of Materials Science and Engineering, The Ohio State University, Columbus, OH 43210. STEPHEN R. NIEZGODA is with the Department of Materials Science and Engineering, The Ohio State University and also with the Department of Mechanical and Aerospace Engineering, The Ohio State University, Columbus, OH 43210. Contact e-mail: niezgoda.6@osu.edu

Manuscript submitted August 17, 2021, accepted October 23, 2021. Article published online November 22, 2021

Medium to high stacking-fault energy (SFE) FCC metals develop a pronounced cube texture after cold rolling followed by recrystallization annealing. [7–9] Although the observation of strong cube texture is universal, its origin has been strongly debated in the last century. Various competing theories such as, 'oriented nucleation', [7,8,10,11] 'oriented growth', [12] 'micro growth', and 'orientation pinning', were proposed to explain the sharp cube texture development after recrystallization. Currently, it is believed that both preferential nucleation and preferential growth contribute to the cube texture development. [15–17] However, many issues regarding the deformation and nucleation of the cube-oriented recrystallized grains are still unresolved.

In regard to the deformation, evolution of the cube component during deformation of polycrystalline aggregate is still not well understood. From previous experimental studies on copper and aluminum, it is known that cube-oriented grains are metastable under plane strain compression<sup>[18,19]</sup> and only a smaller fraction of the cube-oriented grains are retained in the deformed state. On the other hand, Dillamore and Katoh<sup>[20]</sup> suggested that cube-oriented transition bands can

originate from the grains which were rotated about the normal direction (ND). However, the stability of the cube orientation about ND rotation was questioned by Driver et al.[18,21] and by Wert et al.[22] Other experimental studies showed that cube orientations can also originate from S-oriented ( $\{123\}\langle 63\overline{4}\rangle$ ) grains.<sup>[23,24]</sup> However, these experimental studies were mainly conducted using single crystals, hence, it is still unknown how the cube component evolves in a polycrystalline aggregate. Recently, Quey et al. [25] and Albou et al. [26] used electron back scatter diffraction (EBSD) technique to track 176 grains on an internal surface of a polycrystalline sample and found that 3 rotated cube grains, which are rotated about the normal direction (ND) and the transverse direction (TD), developed the cube component at strain of 1.2. Although these results are important, they suffer from the following major issues, (i) these are only two dimensional (2D) observations, (ii) the number of grains studied is too small to fully understand which types of grains are more likely to develop the cube component during deformation and (iii) the stability of the cube component developed during deformation was not analyzed. To overcome these challenges, three dimensional (3D) in-situ characterization techniques, e.g. 3D X-ray diffraction (3D-XRD) or high energy diffraction microscopy (HEDM), will be required. However, in-situ characterization upto large plastic strain is still not possible using these 3D techniques. Alternatively, full field crystal plasticity models can provide 3D in-situ information of the local orientation changes up to large strain. Therefore, it can provide useful information regarding the grain orientations which develop the cube component during deformation as well as evolution and stability of this cube component.

Regarding the nucleation of recrystallized grains. currently there is no consensus on the preferential nucleation sites for the cube-oriented grains. Dillamore and Katoh<sup>[20]</sup> suggested that cube-oriented transition bands are the preferred sites for nucleation. On the other hand, Samajdar and Doherty<sup>[11,14,27]</sup> reported that cube-oriented nuclei originate from the deformed cube bands or debris of the initial cube grains. They proposed a differential stored energy based mechanism for the origin of cube nuclei from the deformed cube bands. Similarly, Zaefferer *et al.*<sup>[28]</sup> reported nucleation of recrystallized cube grains from the cube bands retained in the initial cube grains. In their case, higher misorientation across the cube band was attributed to the origin of the cube-oriented nuclei. According to Albou et al., [26,29] cube bands developed in the rotated cube grains have higher efficiency of nucleation due to the presence of grain boundaries with high mobility. In contrast, Sukhopar *et al.*<sup>[30]</sup> investigated the nucleation propensity of two different types of cube bands and found that cube bands retained in the initial cube grains had higher efficiency than the cube bands formed in other grains. Therefore, it is still unclear which cube

component is favorable for nucleation. In this regard, understanding the evolution of the cube component during cold rolling and analyzing the stored energy difference and disorientation angle with its neighbors are key to understand the preferential nucleation of the cube-oriented recrystallized grains. 3D methods such as full field crystal plasticity simulations can provide such information of the local neighborhood up to large strain

Previously, only few crystal plasticity simulation studies focussed on the cube texture development. [31–35] However, they do not provide information on the different types of cube band, their origin, stability and neighborhood. Additionally, all these simulations did not consider dislocation density as an internal variable. It has been shown that the localization of dislocation density is better predicted by the dislocation density based model than the phenomenological model.<sup>[36]</sup> Further, nucleation models used in the previous works excluded the combined effect of dislocation density and disorientation angle on the nucleation. Hence, in this study, we use a full-field crystal plasticity model coupled with a dislocation density based constitutive theory to study the large strain deformation process in polycrystalline copper under plane strain compression. To precisely capture the hardening and recovery mechanisms up to large strain, we implemented an anisotropic interaction strength matrix (see Table I) for the different dislocation junction forming interactions and included pipe diffusion controlled dislocation climb in our constitutive model. Using this model, we study the evolution and orientation stability of the cube component with deformation and explore the possible grain orientations which develop the cube component during deformation. Lastly, neighborhood of the cube components are analyzed to understand the propensity for nucleation during recrystallization.

# II. MODELING FRAMEWORK

For this work, we utilized an Elasto-Viscoplastic Fast Fourier Transform (EVP-FFT) based crystal plasticity solver based on the work of Lebensohn *et al.*<sup>[37]</sup> Recently, FFT based solvers have emerged as robust tools for studying microstructure based mechanical problems. More details on the numerical implementation of FFT based crystal plasticity models can be found in the recent review articles of Roters *et al.*<sup>[41]</sup> and Lebensohn and Rollett. The FFT implementation along with the necessary input files to reproduce the simulation results can be found on the authors repository (https://github.com/mesoOSU/SRX).

# A. Dislocation Density Based Constitutive Model

In this work, we considered perfect dislocations with  $\frac{1}{2}\langle 110 \rangle$  type Burgers Vector and  $\{111\}$  slip planes. In

case of FCC metals, 12 independent slip systems are present. The total dislocation density is divided into two parts, *i.e.* mobile  $(\rho_m)$  and immobile  $(\rho_{im})$  dislocation density. We note that the constitutive model described below is valid for each spatial point of the 3D volume, therefore, explicit spatial dependence of the constitutive equations is dropped in the remaining text for ease of reading. Slip activity is described by the Orowan equation, [43]

$$\dot{\gamma}^{\alpha} = \rho_{m}^{\alpha} b v^{\alpha} \tag{1}$$

where  $\dot{\gamma}^{\dot{\alpha}}$  is the shear strain rate,  $\rho_m^{\alpha}$  is the mobile dislocation density, b is the Burgers vector and  $v^{\alpha}$  is the velocity of the mobile dislocations for slip system  $\alpha$ . Dislocation motion is assumed to occur via thermally activated glide of mobile dislocations through the short range obstacles (e.g. forest dislocations) on the slip plane. Then the velocity  $v^{\alpha}$  can be expressed as a thermally activated rate equation, [46,47]

$$\rho_P^{\alpha} = \sum_{\beta = \text{self,coplanar}} \chi_{\alpha\beta} \left( \rho_{im}^{\beta} \right)$$
 [6]

As  $\rho_m^{\alpha}$  is orders of magnitude smaller than  $\rho_{im}^{\alpha}$ , we ignored the contribution of  $\rho_R^{\alpha}$  for the calculation of  $\rho_F^{\alpha}$  and  $\rho_F^{\alpha}$ . In Eqs. [4] and [6],  $\chi_{\alpha\beta}$  is the interaction matrix describing strength of the dislocation interaction between slip system  $\alpha$  and  $\beta$ . Interaction between dislocations plays an important role in strain hardening, therefore, the interaction strength parameters ( $\chi_{\alpha\beta}$ ) need to be carefully chosen. In this regard, Jackson and Basinski<sup>[49]</sup> and Franciosi *et al.*<sup>[50]</sup> performed specialized experiments to estimate latent hardening in copper single crystals. They found that latent hardening between different slip systems remain anisotropic where the junction forming interactions (*i.e.* Lomer–Cottrell and glissile junction) are stronger than the non-junction forming interactions (*i.e.* coplanar, collinear and Hirth interaction). Additionally, they

$$v^{\alpha} = \begin{cases} \frac{1}{2} \lambda^{\alpha} f \exp\left(-\frac{Q_{\text{slip}}}{kT} \left(1 - \frac{\left|\tau_{\text{app}}^{\alpha}\right| - \tau_{\text{pass}}^{\alpha}}{\tau_{\text{cut}}^{\alpha}}\right)\right) \operatorname{sgn}\left(\tau_{\text{app}}^{\alpha}\right), & \text{when } \left|\tau_{\text{app}}^{\alpha}\right| > \tau_{\text{pass}}^{\alpha} \\ 0, & \text{when } \left|\tau_{\text{app}}^{\alpha}\right| \leq \tau_{\text{pass}}^{\alpha} \end{cases}$$
[2]

where f is the jump frequency which is in the order of  $10^{10}/\text{s}$  and  $Q_{\text{slip}}$  is the activation energy required to overcome the obstacle which may vary in the range of 0.2 to  $0.5 \, \mu b^3$  for dislocation forest type obstacles, [48] k is the Boltzmann constant and T is the temperature.  $\lambda^{\alpha}$  is the jump distance,  $\tau^{\alpha}_{\text{app}}$  is the resolved shear stress,  $\tau^{\alpha}_{\text{pass}}$  is the passing stress required to overcome the resistance produced by the in-plane dislocations (self and coplanar) on the slip system  $\alpha$ .  $\tau^{\alpha}_{\text{cut}}$  is the stress required to overcome the short range obstacles without any thermal activation. Here, the jump distance  $\lambda^{\alpha}$  is defined as the mean free path for the mobile dislocations,

$$\lambda^{\alpha} = \frac{1}{\sqrt{\rho_F^{\alpha}}}$$
 [3]

where  $\rho_F^{\alpha}$  is the forest dislocation density for the slip system  $\alpha$  which we define as,

$$\rho_F^{\alpha} = \sum_{\beta \neq \text{self,coplanar}} \chi_{\alpha\beta}(\rho_{im}^{\beta})$$
 [4]

 $\tau_{\rm pass}^{\alpha}$  is defined as,

$$\tau_{\mathsf{pass}}^{\alpha} = \mu b \sqrt{\rho_P^{\alpha}}$$
 [5]

where  $\mu$  is shear modulus and  $\rho_P^{\alpha}$  is the in-plane dislocation density for the slip system  $\alpha$ ,

found that Lomer–Cottrell lock has the highest interaction strength among all the interactions. This is also corroborated by the prevalent observation of stable Lomer–Cottrell junctions during stage II hardening of copper single crystals. [51] Therefore, we used an anisotropic interaction strength matrix (see Table I) following the experimental results. As Franciosi  $et\ al.$  [50] reported the latent hardening values relative to the strength of the self interaction, we chose the self interaction parameter according to the work of Devincre  $et\ al.$  [52] and calculated the other interaction strengths using the ratios reported by Franciosi  $et\ al.$  [50] Further,  $\tau_{cut}^{\alpha}$  is defined as,

$$\tau_{\rm cut}^{\alpha} = \frac{Q_{\rm slip}}{V^{\alpha}}$$
 [7]

where  $V^{\alpha}$  is the activation volume for dislocation glide. Here we write  $V^{\alpha}$  as,

$$V^{\alpha} = c_1 \lambda^{\alpha} b \tag{8}$$

where  $c_1$  represents the obstacle width in units of Burgers vector. For dislocation based obstacles  $c_1$  may vary in the range of 1-10b. [46]

Following the work of Ma and Roters, [46] mobile dislocation density  $\rho_m^{\alpha}$  is approximated as a function of in-plane and forest dislocation density,

$$\rho_m^{\alpha} = \frac{2kT\sqrt{\rho_P^{\alpha}\rho_F^{\alpha}}}{c_1\mu b^3}$$
 [9]

For the evolution of immobile dislocation density, rate of immobilization and annihilation of dislocations need to be considered. Here, we assume that immobilization occurs due to the pinning of mobile dislocations by the forest dislocations. Hence, rate of immobilization can be written as,

$$\dot{\rho}_{im+}^{\alpha} = c_2 |\dot{\gamma}^{\alpha}| \sqrt{\rho_F^{\alpha}}$$
 [10]

where  $c_2$  is a constant for the rate of immobilization. On the other hand, an immobile dislocation can be annihilated by a mobile dislocation of opposite sign moving on the same glide plane. The in-plane annihilation is written as,

$$\dot{\rho}_{im-}^{I\alpha} = -c_3 |\dot{\gamma}^{\alpha}| \rho_{im}^{\alpha}$$
 [11]

where  $c_3$  is a constant for in-plane annihilation.

In case of large strain plastic deformation, significant amount of point defects (*e.g.* vacancies) can be generated along with large dislocation density. [53,54] Although vacancy migration through lattice is very slow at room temperature, dislocation cores can provide a short-circuit network for fast vacancy migration, which is commonly known as pipe diffusion. [55,56] Hence, dislocation climb controlled annihilation may occur at room temperature through vacancy migration along the dislocation cores. Rate of dislocation climb controlled annihilation can be written as,

$$\dot{\rho}_{im-}^{II\alpha} = -\frac{1}{2} d_{cl}^{\alpha} v_{cl}^{\alpha} \left(\rho_{im}^{\alpha}\right)^2$$
 [12]

where  $d_{cl}^{\alpha}$  is the mean climb distance and  $v_{cl}^{\alpha}$  is the velocity at which an edge dislocation can climb. We approximate  $d_{cl}^{\alpha}$  as the mean distance at which stable dipoles can form between two edge dislocations.  $d_{cl}^{\alpha}$  is defined as, [46]

$$d_{cl}^{\alpha} = \frac{\sqrt{3}\mu b}{16(1-\nu)\pi|\tau_{app}^{\alpha}|}$$
 [13]

where *v* is the Poisson's ratio. Following References 57, 58, velocity of climb is written as,

$$v_{cl}^{\alpha} = \frac{D}{b} \left( \exp\left(\frac{\sigma_c^{\alpha} V^{cl}}{kT}\right) - 1 \right)$$
 [14]

where D is the effective self-diffusivity,  $\sigma_c^{\alpha}$  is the normal stress acting on an edge dislocation in a dipolar arrangement where the stable dipole distance is  $d_{cl}^{\alpha}$  and  $V^{cl}$  is the activation volume for dislocation climb which is generally taken as  $b^3$ . Therefore, following References 41, 57 we can write,

$$\sigma_c^{\alpha} = \frac{\mu b}{\pi (1 - v) d^{\alpha}}$$
 [15]

D can be written as, [59]

$$D = D^L + A\rho^{\text{tot}}D^P$$
 [16]

where  $D^L$  is the diffusivity corresponding to the lattice diffusion,  $D^P$  is the diffusivity corresponding to the pipe diffusion, A is the effective cross-sectional area for diffusion through dislocation core and  $\rho^{\text{tot}}$  is the total dislocation density. The term  $A\rho^{\text{tot}}$  defines the fraction of short-circuit path available for the pipe diffusion.  $\rho^{\text{tot}}$  is defined as,

$$\rho^{\text{tot}} = \sum_{\alpha=1}^{12} \left( \rho_{im}^{\alpha} + \rho_{m}^{\alpha} \right)$$
 [17]

Activation energy for pipe diffusion typically ranges from 0.4 to 0.7 times of the activation energy for lattice diffusion in FCC metals. [55] Hence,  $D^P$  can be orders of magnitude higher than  $D^L$  at room temperature. Values of  $D^L$  and  $D^P$  can be estimated from the previous experimental works of References 60 and 61, respectively. For the calculation of A, pipe radius of 6b is assumed. [62]

Finally, using Eqs. [10], [11] and [12], the rate of change of immobile dislocation density can be written as,

$$\dot{\rho}_{im}^{\alpha} = \dot{\rho}_{im+}^{\alpha} + \dot{\rho}_{im-}^{I\alpha} + \dot{\rho}_{im-}^{II\alpha}$$
 [18]

Values of all the model parameters are given in Table II.

# III. RESULTS AND DISCUSSIONS

In this work, we utilized open source Dream.3D software<sup>[63]</sup> to construct two representative volume elements (RVE) each containing 128 × 128 × 128 grid points on an equi-spaced rectilinear grid, i.e. more than 2 million grid points in each RVE. The purpose of using two different RVEs is to understand the effect of variation in initial texture and grain neighborhood on the development of cube component during deformation. The first RVE contains 520 grains with log-normal distribution of grain size and almost uniform distribution of misorientation angle with the peak near 45 deg (see Figure 1), we call it 'M1'. The second RVE contains 479 grains with log-normal distribution of grain size and weakly cube texture (refer to Figures S-1 and S-4 in electronic supplementary material), we call it 'M2'. Such weakly cube textured microstructure has been used in the previous recrystallization studies of copper. [64,65] Both M1 and M2 have nearly equiaxed grain morphology (see Figure 2 for M2). Crystal plasticity model parameters,  $c_1$  to  $c_3$ , were obtained by calibrating the simulated stress-strain response with an uniaxial compression stress strain data available in the literature. [66] Plane strain compression simulations with RVE M1 and M2 were performed using the same parameters. Refer to

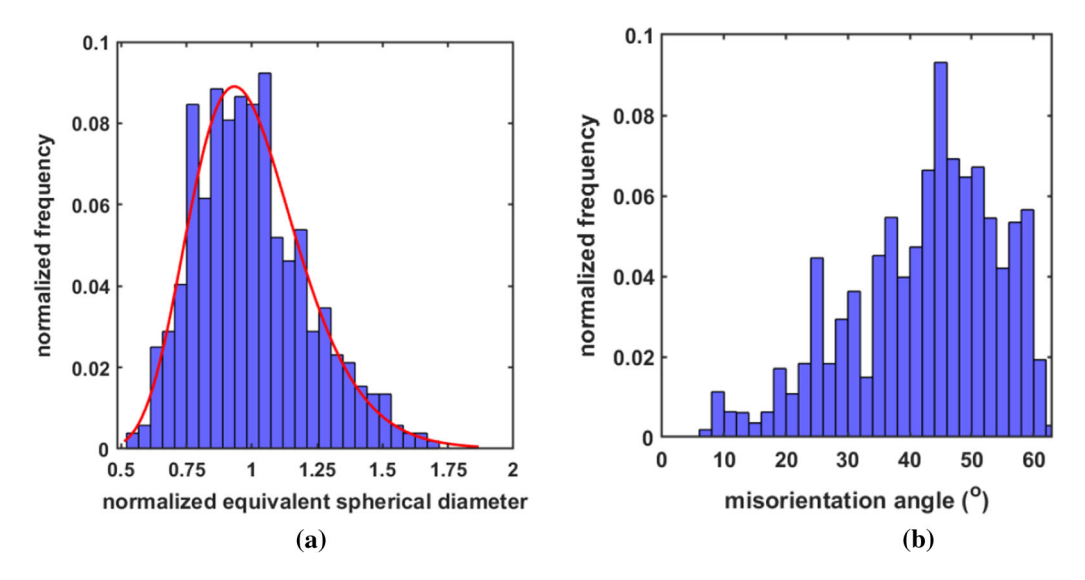


Fig. 1—(a) Grain size distribution and (b) misorientation angle distribution in RVE M1. Log-normal fit for the grain size distribution is also shown with red curve in (a). The misorientation angle distribution is almost uniform with the peak near 45 deg.

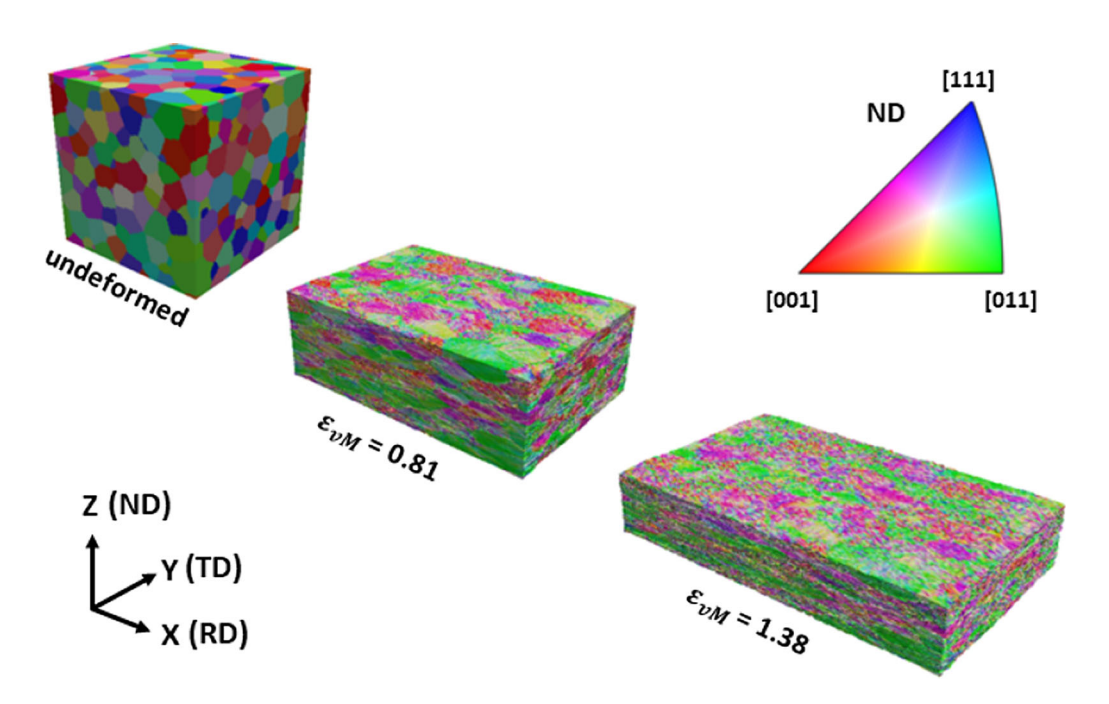


Fig. 2—Three dimensional (3D) view of the deformation process and texture evolution during plane strain compression in M2.

Table I. Dislocation Interaction Strengths Used for  $\frac{\text{Copper}^{[50,52]}}{\text{Copper}^{[50,52]}}$ 

Interaction	Χαβ
Self	0.1
Coplanar	0.125
Hirth Junction	0.1
Glissile Junction	0.15
Collinear	0.125
Lomer-Cottrell Junction	0.2

Figures S-2 and S-3 in the supplementary material for more details on the model calibration and mean dislocation density evolution.

# A. Deformation Texture Evolution

All the texture analyses were performed using the open source MTEX software.<sup>[69]</sup> A list of main texture components along with their Miller indices and Euler

angles are given in Table AI. Figure 2 shows the deformation texture evolution in the 3D microstructure. For more detailed analysis, we calculated the orientation distribution function (ODF) using De La Vallee Poussin kernal with a halfwidth of 5 deg. Figure 3 shows the calculated ODFs for M1 in the undeformed state and after von Mises strain  $(\epsilon_{vM})$  of 1.38 which is equivalent to 70 pct thickness reduction in plane strain compression. The initial texture was nearly uniform, whereas, the deformed texture clearly shows high intensity of the copper and the S texture components and lower intensity of the brass components. The deformation texture is similar to the 'copper' type texture which is commonly observed for plane strain compression of medium to high stacking-fault energy FCC metals. [70-72] ODF calculated for the deformed M2 is similar to the ODF of deformed M1, which is shown in Figure S-4 in the supplementary material. As the purpose of the present study is to understand the evolution of the cube component during deformation, we limit our discussion of the overall texture here and focus on the cube component in the following sections.

# B. Evolution of the Cube Component

In Figure 4(a) we present longitudinal (ND-RD) sections of the undeformed and deformed (at  $\epsilon_{vM} = 0.81$ and 1.38) microstructure. Figure 4(a) shows the inverse pole figure maps, whereas, Figure 4(b) shows the angular deviation from the ideal cube orientation. In this figure, two types of cube component in the deformed state can be easily distinguished when compared with the undeformed state, (i) the cube component retained in the initial cube grains (within 10 deg angular deviation from the ideal cube orientation) and (ii) the cube component developed in the initial non-cube grains (> 10 deg angular deviation from the ideal cube orientation). From here we will call the first type of cube component as the 'cube-I' and the second type as the 'cube-II'. Some of the cube-I and cube-II are marked with black and white arrows, respectively.

The noticeable features of these cube components are as following: (1) In general, both the cube components are located near the intergranular regions, however, some are also located in the intragranular regions; (2) cube components of both the types become thinner with increasing deformation and mostly retained as tiny fragments in the deformed microstructure, although band-like elongated structures can also be observed in few locations. In Figures 4(a) and (b), two such regions are highlighted with white boxes and labeled as 'A' and 'B'. Area 'A' contains a cube band of type II, whereas, area 'B' contains a cube band of type I. Orientation

distribution corresponding to both the areas 'A' and 'B' are also presented in {111} pole figures in Figure 5, which clearly shows the presence of near cube orientations.

Figure 6 shows the evolution of volume fraction of the cube-I and the cube-II with increasing deformation. During the initial stages of deformation (up to  $\epsilon_{vM}$  = 0.46), volume fraction of the cube-I rapidly decreases, whereas, volume fraction of the cube-II increases. Beyond this stage of deformation, volume fraction of both the cube components slowly decreases. In case of M1, at  $\epsilon_{vM}$  of 1.38 (i.e. 70 pct thickness reduction), only 0.02 and 0.26 pct of the total volume were retained in the cube-I and the cube-II, respectively. On the other hand, in M2, only 0.07 pct and 0.29 pct of the total volume were retained in the cube-I and the cube-II, respectively at the same deformation level. Therefore, relative fraction of the cube-I and the cube-II vary depending on the initial texture and the level of deformation. Here, cube-II became the dominating component at larger deformation for both the microstructures, hence, it is necessary to analyze its origin during the deformation and its role in the recrystallization process.

# C. Development of Cube Component in the Non-cube Grains

# 1. Comparison with experiments

Albou et al. [26] tracked three different non-cube grains which developed the cube component at strain of 1.2 during hot plane strain compression of aluminum. Even though they only performed EBSD based surface observation and grains in the experimental setup may have different neighborhood than the grains in the simulation study, their findings are useful for comparison with the simulation results. However, there are some inherent differences between aluminum and copper which must be discussed before the comparative study. Even though both aluminum and copper are considered as medium to high SFE FCC metals, aluminum has much higher SFE  $(\approx 200 \, mJ/m^2)$  than copper  $(\approx 78 \, mJ/m^2)$ . [15] SFE influences the strain hardening as well as dynamic recovery during the deformation of FCC metals. A stronger latent hardening effect in copper than in aluminum has been by Franciosi *et al.*<sup>[50]</sup> Similarly, cross slip controlled recovery can be less pronounced in copper than it is in aluminum. Apart from that, aluminum has much lower elastic anisotropy (anisotropy ratio 1.21<sup>[73]</sup>) than copper (anisotropy ratio 3.2.<sup>[67]</sup>) Additionally, non-octahedral slip activity has been reported during hot deformation of aluminum

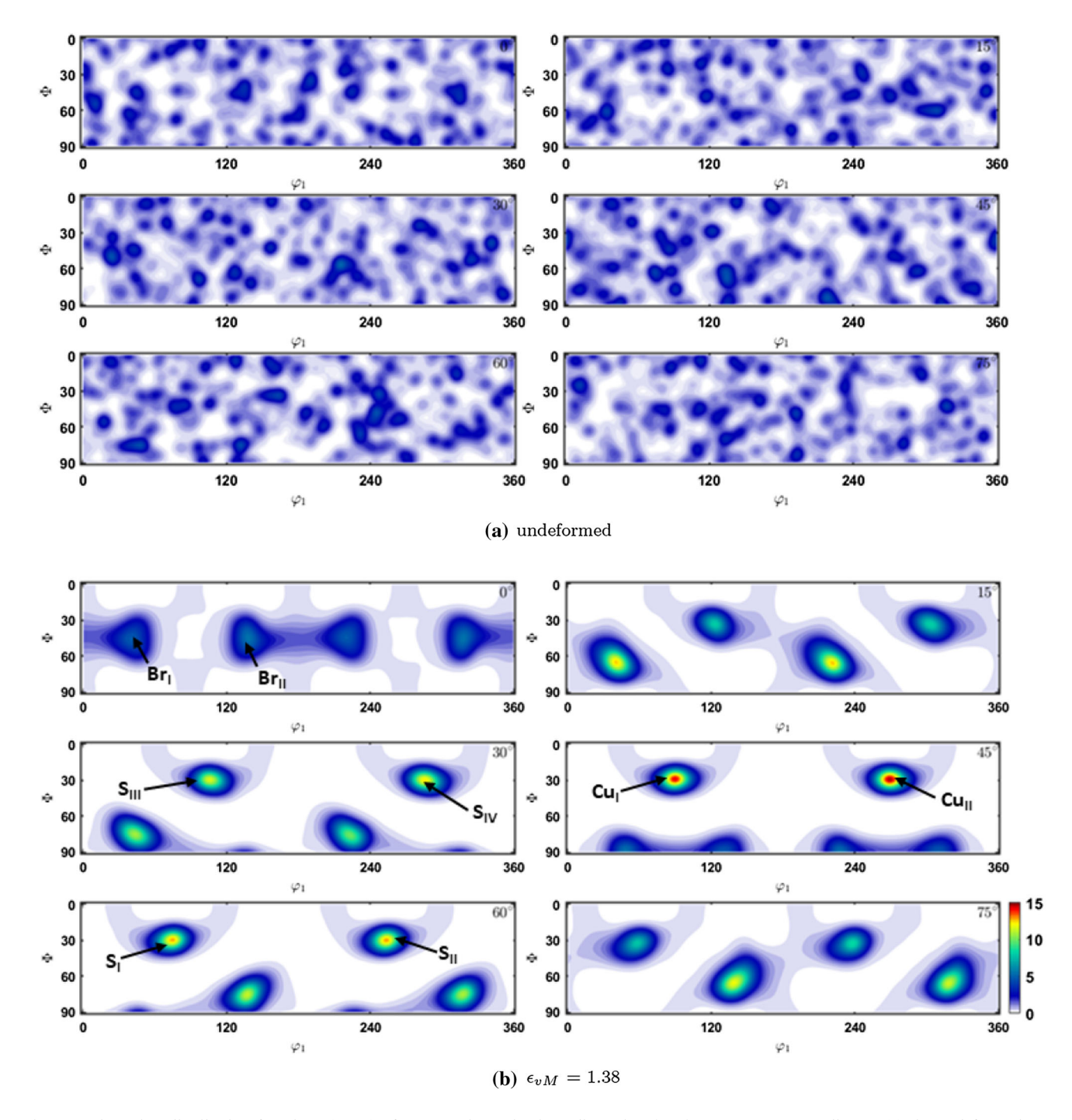


Fig. 3—Orientation distribution functions (ODF) of M1 are shown in three dimensional Euler space, corresponding to (a) the undeformed state and (b) the deformed state at  $\epsilon_{vM}$  of 1.38. Bunge convention is used to represent the orientations. Texture is almost uniform in the undeformed state, whereas, a typical 'copper' type texture with intensities near the copper, S and brass components is clearly visible after deformation. The variants of copper, S and brass components are also shown using black arrows.

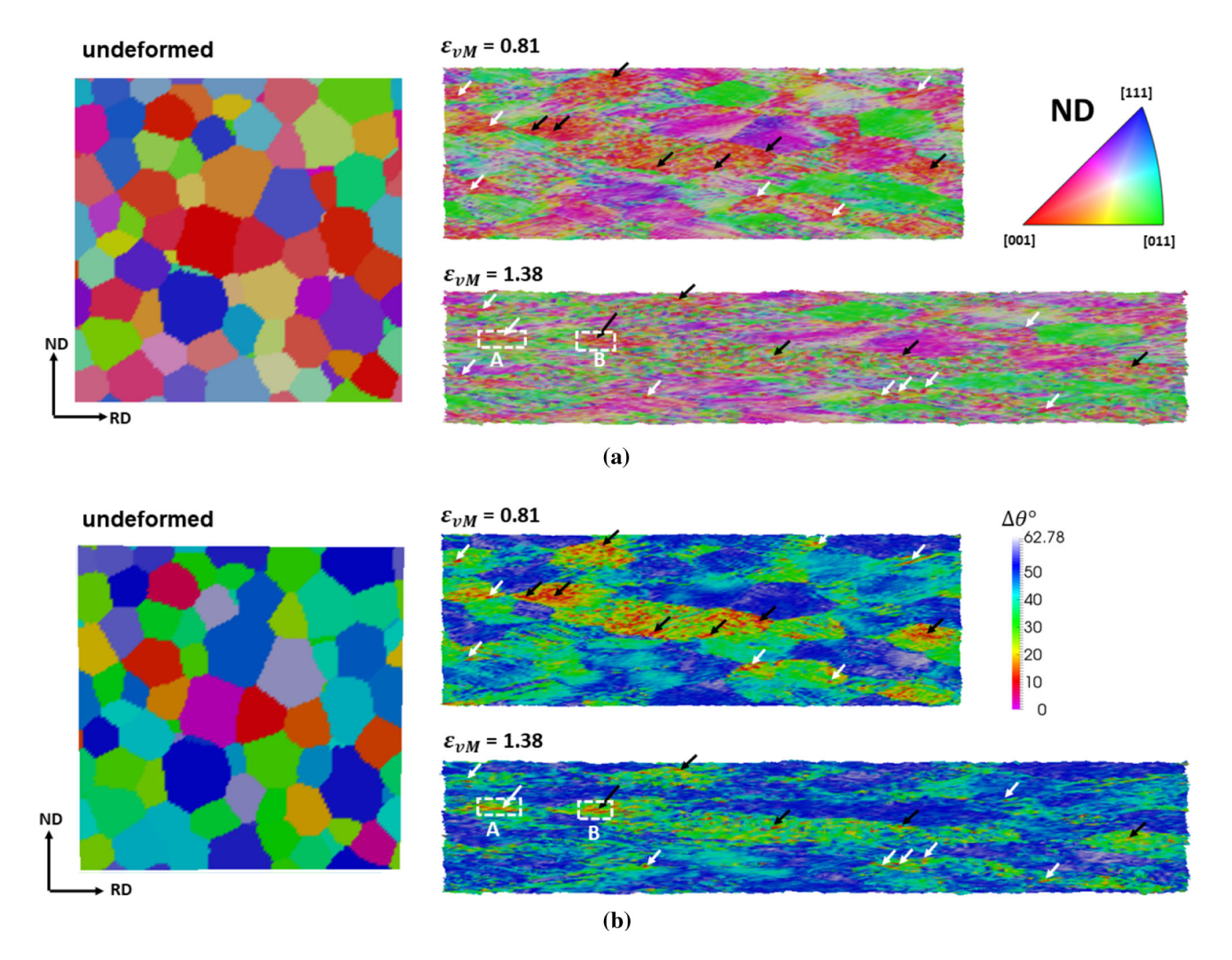


Fig. 4—ND-RD sections of M2 showing the (a) inverse pole figure maps and (b) angular deviation  $(\Delta\theta)$  from the ideal cube orientation in the undeformed state (left), at  $\epsilon_{vM}=0.81$  (right top) and at  $\epsilon_{vM}=1.38$  (right bottom). Black arrows show the cube component retained in the initial cube grains (cube-I) and white arrows show the cube component originated from the initial non-cube grains during the deformation (cube-II). Both the cube components become thinner with increasing deformation and retain mostly near the intergranular regions, although some intragranular fragments can also be observed. Few elongated cube bands are also visible in the deformed state of strain 1.38. Two such regions are marked with white boxes and labeled as 'A' and 'B'.

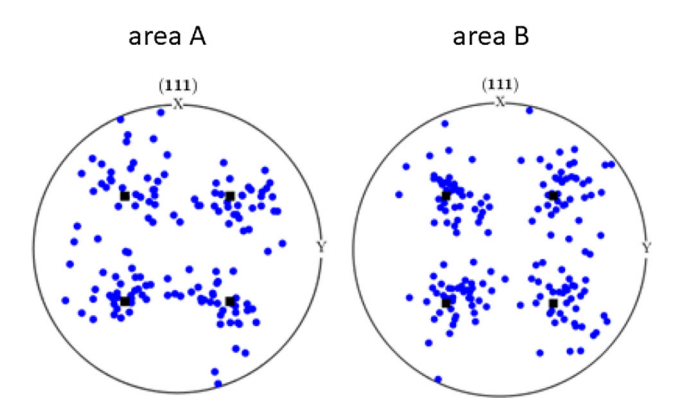


Fig. 5— $\{111\}$  pole figures showing the orientations corresponding to the area 'A' and 'B' as highlighted in the Figure 4. The ideal cube orientation is also shown with the black square shaped markers. X and Y are the sample RD and TD directions, respectively. Orientations near the ideal cube is clearly visible in both 'A' and 'B'.

which influences the stability of the near brass and the near cube grains. [74,75] As a result, local deformation process and micro-texture evolution might differ during deformation of copper and aluminum, even though the macro-texture evolution during rolling of copper and aluminum do not differ significantly (both show a typical 'copper-type' texture [70,71]). A future work must be conducted to understand the similarities and differences between the local deformation behavior of copper and aluminum. In this regard, the dislocation density based crystal plasticity model can be utilized.

Figure 7 shows the initial orientation of the three grains tracked in the experiment (marked with red star) and the initial orientation of the corresponding grains tracked in the simulation study (marked with blue dot) in {111} pole figures. From the angle-axis description of the grains in the simulation given in

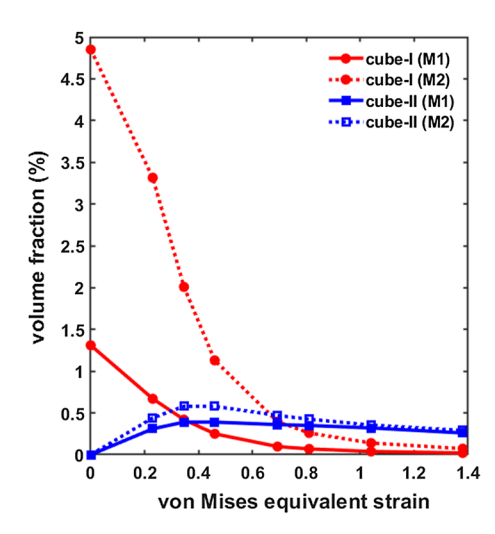


Fig. 6—Evolution of the cube component retained in the initial cube grains (cube-I) and the cube component originated from the non-cube grains (cube-II) with increasing deformation in two different microstructures M1 and M2.

Table AII, we deduce that G1 is a near ND-rotated cube grain, G2 is a near TD-rotated cube grain and G3 is a mixed ND-RD rotated cube grain. All the three grains G1, G2 and G3 belong to RVE M1. Figure 8 shows the grain-scale texture development for all the three grains at  $\epsilon_{vM}$  of 1.38 in both ND and RD inverse pole figure maps. For the sake of comparison with the experimental results, [26] a halfwidth of 3 deg is used to calculate the ODF for the simulation results as well. Different rolling texture components are shown with different colors (cube: red, brass: green, copper: yellow, S: blue) in both 3D and 2D sections of the deformed grains. In this regard, all the texture components are shown within 10 deg angular spread to avoid significant overlap between the rolling texture components. To reveal the full angular spread, 2D misorientation maps of the copper, S and brass components are also provided in Figure S-5 in the supplementary material.

Similar to the experiment, [26] all the three grains in the simulation show the cube oriented fragments along with

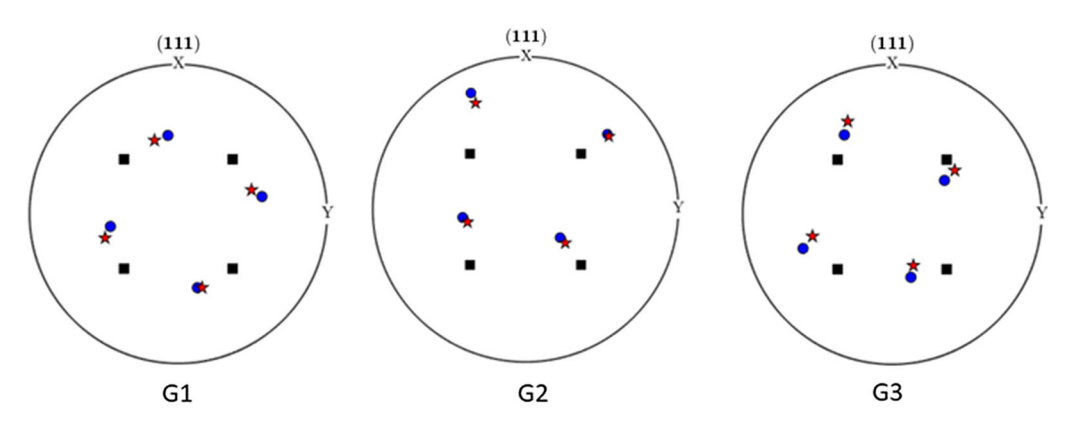


Fig. 7—Initial orientation of the three grains tracked in the experiment [26] and in the simulation are shown in  $\{111\}$  pole figure. Equal angle projection. The sample coordinate axes X and Y represents the rolling direction (RD) and the transverse direction (TD), respectively. Red star shaped markers are used to show the grain orientations tracked the experiment, blue markers are used to show the grain orientations tracked in the simulation. The ideal cube orientation is also shown using the black square shaped markers (Color figure online).

Table II. Crystal Plasticity Model Parameters for Copper

Parameter	Definition	Value
$\overline{C_{11}}$	elastic stiffness coefficients	168.4 GPa <sup>[67]</sup>
$C_{12}$		121.4 GPa <sup>[67]</sup>
$C_{44}$		75.4 GPa <sup>[67]</sup>
ν	Poisson ratio	$0.33^{[68]}$
$\mu$	shear modulus	47.5GPa <sup>[68]</sup>
$Q_{slip}$	activation energy for slip	$2.0 \times 10^{-19} \text{ J}^{[48]}$
b	Burgers vector	$2.556 \times 10^{-10} \text{ m}^{[68]}$
$ ho_{im}^{lpha,initial}$	initial immobile dislocation density	$10^{12} / \text{m}^2$
f	dislocation jump frequency	$10^{10} / s^{2[45]}$
T	temperature	300 K
$c_1$	obstacle width	1.0b
$c_2$	constant for immobilization	$6.0 \times 10^{8} / \text{m}$
<i>c</i> <sub>3</sub>	constant for in-plane annihilation	17.0
$D^L$	lattice diffusion coefficient	$3.8 \times 10^{-40} \text{ m}^2/\text{s}^{[60]}$
$D^P$	pipe diffusion coefficient	$2.4 \times 10^{-20} \text{ m}^2/\text{s}^{[61]}$
A	effective cross-sectional area for pipe diffusion	$10^{-17} \text{ m}^{2[62]}$

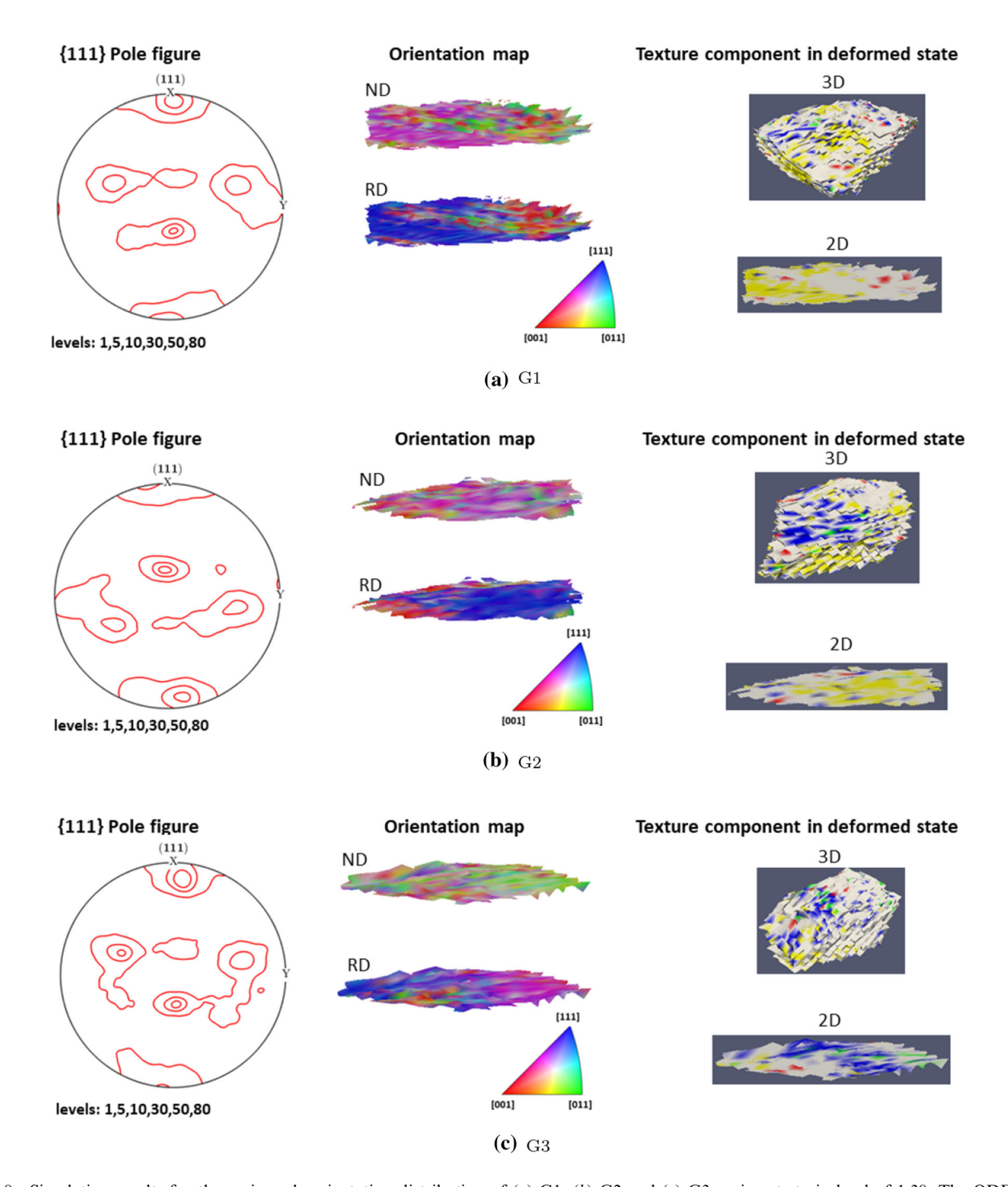


Fig. 8—Simulation results for the grain-scale orientation distribution of (a) G1, (b) G2 and (c) G3 grains at strain level of 1.38. The ODFs are calculated using 3 deg halfwidth and are shown in  $\{111\}$  pole figures. Equal angle projection is used. The sample coordinate axes X and Y represents the RD and TD directions, respectively. The following color scheme is used for visualization of the texture components within 10 deg angular tolerance; red: cube, yellow: copper, blue: S, green: brass and white: others (Color figure online).

the copper and the S components in the deformed state. Additionally, the orientation spread for all the grains, as shown in the pole figures, match reasonably well with the orientation spread shown in the experimental work.

Hence, our full field crystal plasticity model is able to capture the grain specific lattice rotations and development of the cube component quite well. Moreover, our model successfully demonstrates that the development of the cube component is not restricted to ND-rotated cube grains, rather grains with other orientations can also develop the cube component during deformation.

# 2. Favorable grain orientations for the development of cube-II

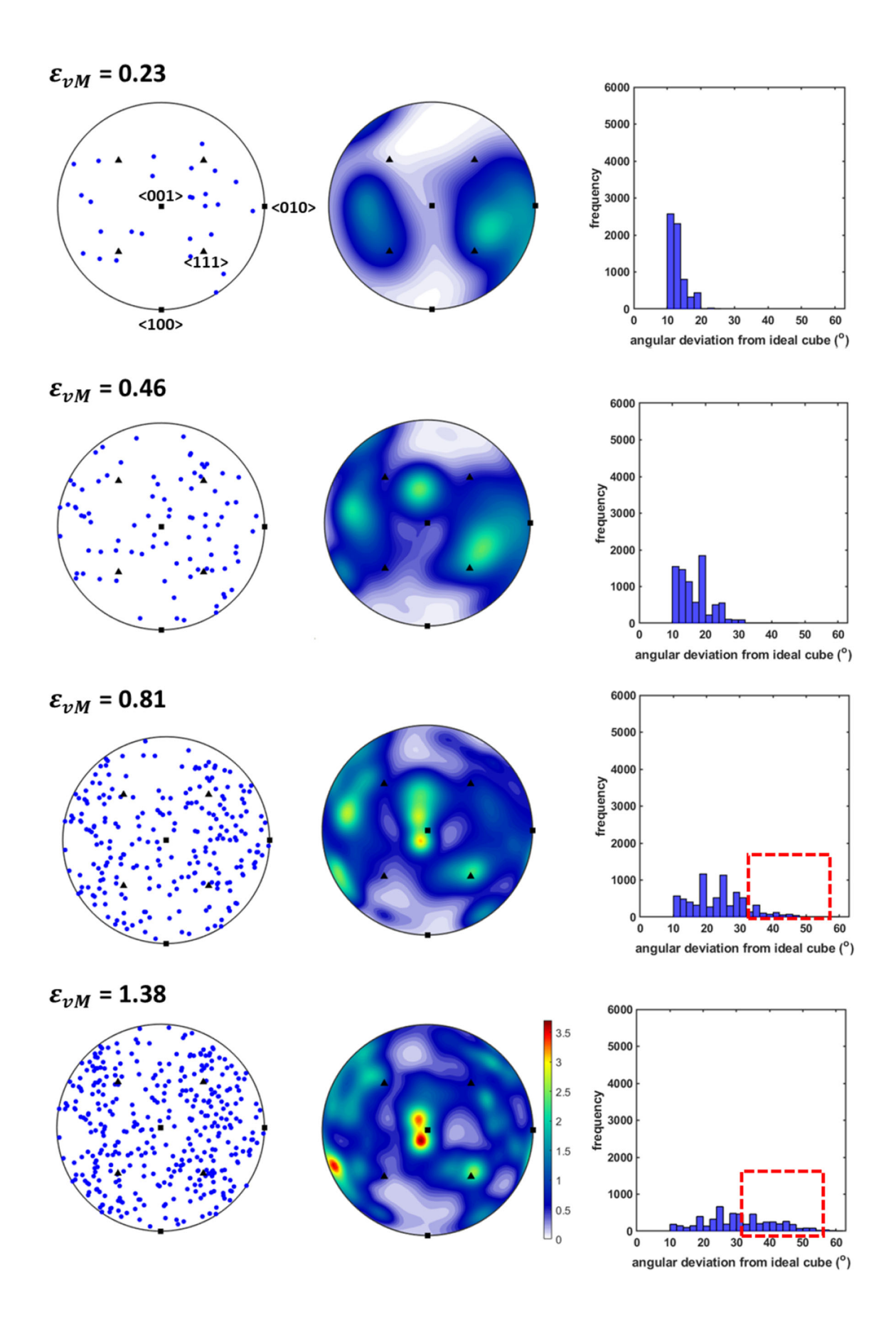
Although the model successfully predicted the development of cube component in three non-cube grains, we still do not know which grain orientations are likely to develop the cube component during deformation. To answer that question, we trace the initial grain orientations corresponding to each of the locations where the cube-II is found at  $\epsilon_{vM}$  of 0.23, 0.46, 0.81 and 1.38, respectively. Next, we calculate the ODF using all of those initial grain orientations. Figure 9 shows the axis-angle distribution corresponding to all the noncube grains in M1 which develop cube-II at various strain levels. At strain level of  $\epsilon_{vM} = 0.23$ , only few grains which are mostly within 10 to 20 deg from the ideal cube orientation, develop the cube component during deformation. For these grains, only a weak preference for near <111> and <011> orientation axes are visible, which are of mixed ND, TD and RD-rotated cube grains. At strain level of  $\epsilon_{vM} = 0.46$ , frequency of the cube-II decreased in the grains which are closer to the ideal cube orientation and increased in the grains with larger angular deviation from the ideal cube orientation. The orientation axes still remain weakly distributed near <111> and <110> axes. At larger strain levels ( $\epsilon_{vM} = 0.81$  and 1.38), higher intensity near the <001> orientation axis is clearly visible, even though many grains with other axes are also present in the distribution. However, frequency of cube-II in the grains with lower angular deviation from the ideal cube orientation continue to decrease, whereas, the frequency of the grains with larger angular deviation from the ideal cube orientation increases. The increase in the frequency of grains with angular deviation higher than 30 deg from ideal cube orientation is highlighted with red boxes for strain levels of  $\epsilon_{vM} = 0.81$  and 1.38. In case of M2, evolution of the angle distribution remains qualitatively similar to the evolution observed for M1, as shown in Figure 10. For axis distribution, only a weak preference for near <111>, <101> and <010> axes is observed at different strain levels.

These results show that the development of cube component in the non-cube grains is dynamic in nature. Grains which are within 10 to 20 deg from the ideal cube orientation, develop the cube component at the early stages of deformation and rotate away from

the cube orientation with increasing deformation. On the other hand, some of the grains with larger angular deviation from the ideal cube orientation tend to rotate towards the cube orientation at large deformation. Even though development of cube orientation in ND-rotated cube grains was postulated by Dillamore and Katoh<sup>[20]</sup> and observed in visco-plastic self consistent modelling,<sup>[34]</sup> the full field modeling results demonstrate that preference for any specific orientation axis is weak during deformation of polycrystalline aggregate and the axis distribution evolves with the amount of deformation. The preference for ND-rotated cube grains (i.e. (001) orientation axis) is observed only in M1 at strain levels of  $\epsilon_{vM} = 0.81$ and 1.38. On the other hand, a weak preference for TD-rotated cube grains is observed in M2 at strain of  $\epsilon_{vM}$  = 1.38. Therefore, the evolution of the cube-II can vary with the variation of microstructure and grain neighborhood. Regarding the development of cube component in the initially S-oriented grains as observed in previous studies, [24,31] our results show that only  $0.7\hat{2}$  and 0.58 pct of the total cube-II were found inside the initially S-oriented grains (within 10 deg angular deviation) of M1 and M2, respectively at strain of  $\epsilon_{vM} = 1.38$ . Moreover, no significant fraction of the total cube-II was found in the grains which belong to the  $\beta$ -fiber. In Figure A1, the ODF for the non-cube grains in M1 which develop the cube component at  $\epsilon_{vM} = 1.38$  is shown in the reduced Euler space along with the full  $\beta$ -fiber as defined by Reference 76.

## 3. Orientation stability of cube-II

To demonstrate the dynamic evolution and the lattice rotations involved in the formation of the cube-II, we tracked the orientation changes in the grain G1, which is a near ND-rotated cube grain. Figure 11(a) shows the rotation path associated with the formation of the cube component at  $\epsilon_{vM}$  of 0.81 in {100} pole figure. Rotation about the ND axis is clearly visible, which is marked with red arrows in this pole figure. With further deformation from  $\epsilon_{vM} = 0.81$  to  $\epsilon_{vM} = 1.38$ , these orientations started to rotate away from the cube component, primarily due to rotations about the TD and RD axes. This result shows the instability of the cube component developed during deformation. The choice of strain level of 0.81 served two purposes in this case: (i) we were able to track the lattice rotations involved during the formation cube component, i.e. rotations from undeformed state to strain of 0.81 and



**◄** Fig. 9—Axis-angle distribution for the non-cube grains (> 10 deg angular deviation from ideal cube) in which the cube component was found at  $\epsilon_{vM} = 0.23$ , 0.46, 0.81 and 1.38, respectively in RVE M1. The individual orientation axes are shown with blue markers. For reference, ⟨001⟩, ⟨010⟩, ⟨100⟩ axes are shown with black square markers and ⟨111⟩ axis is shown with black triangular marker. The ODF is calculated for all the orientations using a halfwidth of 5 deg and the corresponding axis distribution is presented to visualize the intensity of individual axis. The angle distribution is presented in the histogram for each strain levels. Increase in the frequency of higher angles is highlighted with the red boxes at strain levels of 0.81 and 1.38 (Color figure online).

(ii) lattice rotations involved during the rotation away from the cube component, *i.e.* deformation from strain of 0.81 up to 1.38.

To reveal the rotation axes involved in the formation of the cube component and its subsequent instability we plot the orientations in the Rodrigues–Frank (RF) space in Figure 11(b). The ideal cube orientation is located at the origin (0,0,0) of the RF space. More details on the RF space and representation of orientations can be found in the book by Engler and Randle. This figure clearly shows that the orientations initially rotated parallel to the ND axis with a small spread along the TD axis to reach the cube component in the orientation space. From  $\epsilon_{vM} = 0.81$  to 1.38, the orientations spread along the TD and RD axes and move out of the cube component.

# D. Comparison of Nucleation Propensity of the Cube-I and the Cube-II

Nucleation during recrystallization does not occur by random atomic fluctuations as proposed for classical nucleation theory, rather they always originate from the deformed substructure.<sup>[15]</sup> Here, we briefly discuss the possible mechanisms for nucleation during recrystallization, more details can be found in some of the earlier works.[15,78] Numerous TEM studies have confirmed that after large deformation in plane strain compression a cell block type dislocation structure forms where the individual cells are elongated along the rolling direction. During annealing, a recrystallized grain can nucleate if a particular dislocation cell grows abnormally (or discontinuously) and acquire high angle boundaries. This mechanism is also commonly known as 'bulging' or strain induced boundary migration (SIBM).<sup>[79]</sup> Abnormal subgrain growth has been widely adopted as the potential nucleation mechanism in previous static recrystallization works. [80-83] Additionally, bulging of cube-oriented subgrains were also observed in previous experimental works. [7,84]

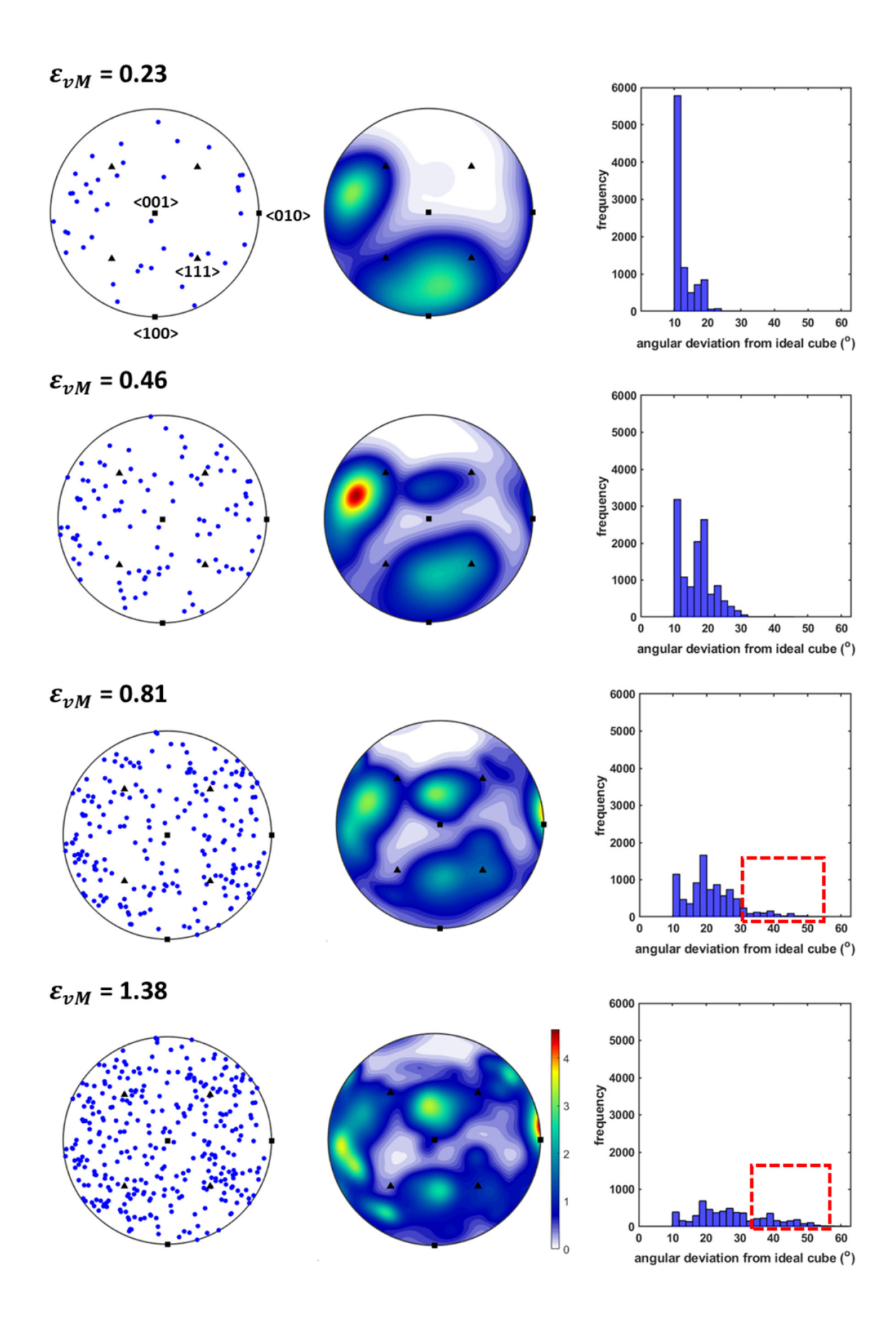
In Figure 12, we schematically present the possible mechanism for nucleation to occur due to discontinuous growth of a dislocation cell during the annealing process. If significant stored energy difference exists across a high angle boundary (HAB) then the cells with lower stored energy (i.e. larger size) can grow into the high stored energy (i.e. smaller cell size) region. The HAB provides sufficient mobility to continue the discontinuous growth, whereas, if only low angle boundaries are present, the nuclei might get pinned due to lack of mobility.[13,14] Recently, the importance of disorientation angle in recrystallization nucleation has been emphasized by References 85, 86. Another theory proposed particularly for preferential nucleation of the cube grains is that the deformed cube bands are located in the neighborhood of S components, hence, the cube oriented cells get an early growth advantage due to higher boundary mobility. [9] In this case, the condition for nucleation shall remain same as SIBM, only the general HAB will be replaced with the special (111)-40 deg boundary.

As the propensity of abnormal growth depends on the neighborhood of a dislocation cell, nucleation propensity of the cube components can be compared using their local dislocation density and neighborhood information. To compare nucleation propensity of the cube components, we calculated dislocation density difference and disorientation angle between each grid point which has cube orientation and its six nearest neighbor grid points at strain of  $\epsilon_{vM}=1.38$ . Dislocation density difference is calculated as following,

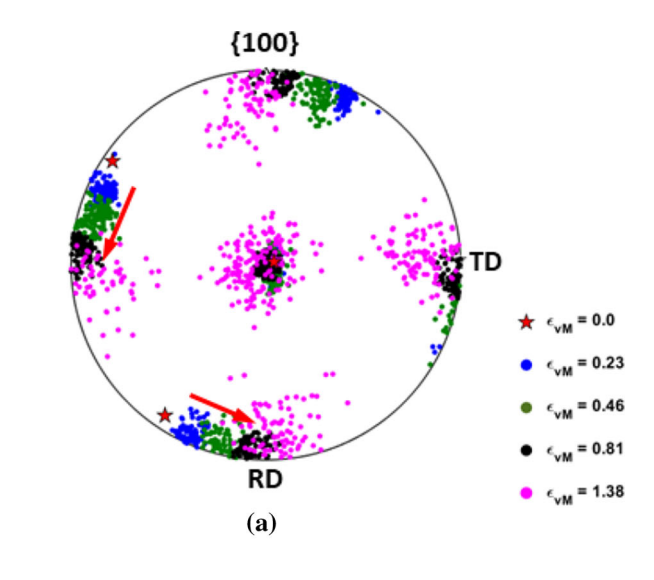
$$\Delta \rho_{ij} = \rho_j^{\text{tot}} - \rho_i^{\text{tot}}$$
 [19]

where  $\rho^{\text{tot}}$  is the total dislocation density defined previously in Eq. [17], i is the grid point of interest and j is one of its nearest neighbor. Therefore, a positive value of  $\Delta \rho_{ij}$  means dislocation density at point i is lower than its neighbor j. For true nucleation preference, a highly positive value of  $\Delta \rho$  is required. Disorientation angle  $(\Delta \theta_{ij})$  is calculated using the MTEX 4.4 software.

Figures 13 and 14 present scatter plots of  $\Delta \rho_{ij}$  and the corresponding  $\Delta \theta_{ij}$  for both the cube components in M1 and M2, respectively. Additionally, histograms of  $\Delta \rho_{ij}$  and  $\Delta \theta_{ij}$  are shown on the left and top of each of the scatter plot, respectively. Green markers are used to specify the S-orientated neighboring grid points. In both M1 and M2, distribution of  $\Delta \rho_{ij}$  for the cube-II is skewed towards negative values. The corresponding scatter plots show that  $\Delta \rho_{ij}$  values are more evenly



 $\blacktriangleleft$  Fig. 10—Axis-angle distribution for the non-cube grains (> 10 deg angular deviation from ideal cube) in which the cube component was found at  $\epsilon_{vM} = 0.23$ , 0.46, 0.81 and 1.38, respectively in RVE M2. The individual orientation axes are shown with blue markers. For reference, ⟨001⟩, ⟨010⟩, ⟨100⟩ axes are shown with black square markers and ⟨111⟩ axis is shown with black triangular marker. The ODF is calculated for all the orientations using a halfwidth of 5 deg and the corresponding axis distribution is presented to visualize the intensity of individual axis. The angle distribution is presented in the histogram for each strain level. Increase in the frequency of higher angles is highlighted with the red boxes at strain levels of 0.81 and 1.38 (Color figure online).



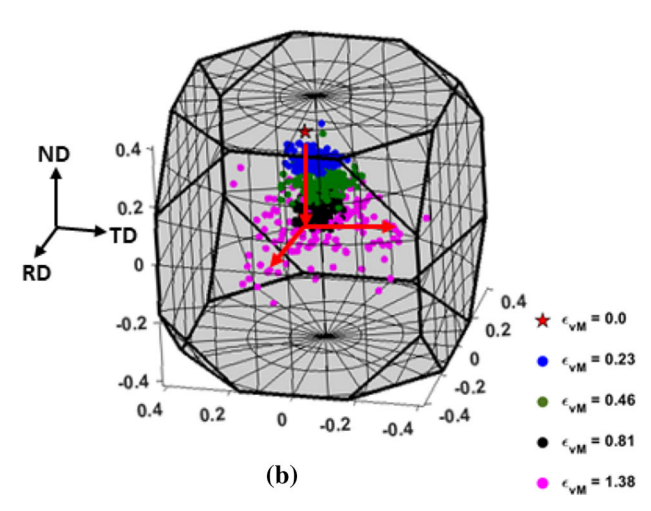


Fig. 11—(a) Lattice rotations associated with the development of cube component in a near ND-rotated cube grain (G1 in Figure 7) is shown in {100} pole figure. Equal angle projection is used. The sample coordinate axes X and Y represents the rolling direction (RD) and the transverse direction (TD), respectively. To understand the instability of the cube component we chose those locations where the cube component is stable at  $\epsilon_{vM}$  of 0.81. Different colors are used to indicate different levels of deformation. Red arrows show the lattice rotation about ND axis. (b) Distribution of the same orientations in the Rodrigues–Frank space. Orientations initially move parallel to the ND axis to reach the cube component and then spread along the TD and RD axes to move out of the cube component. The rotation axes are shown with the red arrows (Color figure online).

distributed between the positive and negative values for cube-I. In comparison to the cube-I, cube-II has higher frequency of S orientation in its neighborhood.

For more quantitative understanding, we define nucleation conditions using different thresholds of  $\Delta\theta_{ii}$  and plot the frequency of both the cube components for different values of  $\Delta \rho_{ij}$  in Figure 15. First, we assume  $\Delta\theta$  greater than 15 deg is required along with a positive  $\Delta \rho$ , we call it relaxed nucleation condition. Second, we assume S-oriented neighbor must be present along with a positive  $\Delta \rho$ , we call it stringent nucleation condition. The disorientation angle with an S-oriented neighbor is always greater than 15 deg (see Figures 13 and 14), while, it imposes an additional constraint of near (111) axis. In case of the relaxed nucleation condition, the cube-II has higher frequency than the cube-I for all the threshold used for  $\Delta \rho$ . However, the preference for the cube-II decreases with increasing threshold of  $\Delta \rho$ . In RVE M2, for  $\Delta \rho$  values above  $1.2 \times 10^{15}/(m^2)$ , frequency of the cube-I becomes comparable to that of the cube-II. In case of the stringent nucleation condition, even though the number of potential nucleus decreases, the trends for the nucleation propensity of both the cube components remain similar to the relaxed nucleation case. Therefore, with both the nucleation conditions, the advantage of the cube-II is clearly visible up to a  $\Delta \rho$  value of  $1.2 \times 10^{15}/(m^2)$ . However, for very stringent nucleation condition such as combination of very high value of  $\Delta \rho$ and S-oriented neighbor, both the cube component show similar nucleation propensity.

As the cube component is a minor texture component in the highly deformed state and both the cube-I and the cube-II retained as narrow bands or fragments in the deformed microstructure (see Figure 4), it is easy to understand that both of them have high disorientation angles in their neighborhood. Hence, their relative volume fraction and  $\Delta \rho$  play more important role in determining the propensity of nucleation between the two cube components. Even though cube-II has lesser advantage than cube-I in terms of  $\Delta \rho$ , cube-II can still play a significant role in nucleating cube oriented recrystallized grains when volume fraction of the cube-I is very low in the deformed state (e.g. M1). On the other hand, both the cube components can play equally important role if a higher fraction of the cube-I is retained in the deformed state (e.g. M2).

## IV. CONCLUSIONS

We used EVP-FFT based crystal plasticity model with dislocation density based constitutive law to simulate the deformation process of copper in plane strain compression. Microstructural evolution of the cube component was analyzed in detail. Grain-scale evolution of the cube component was compared with available experimental results. To understand nucleation propensity, neighborhood of both the cube components were

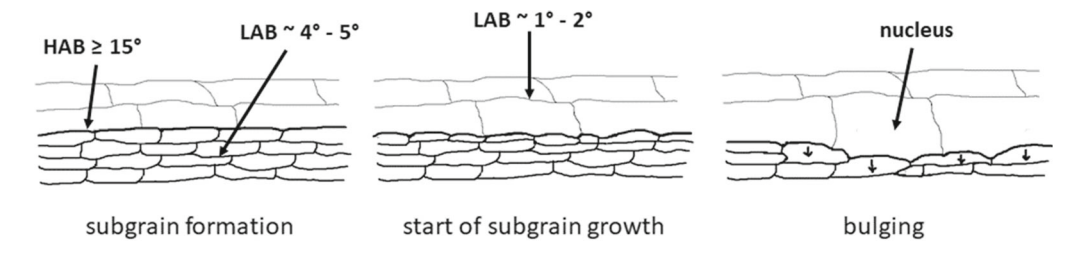
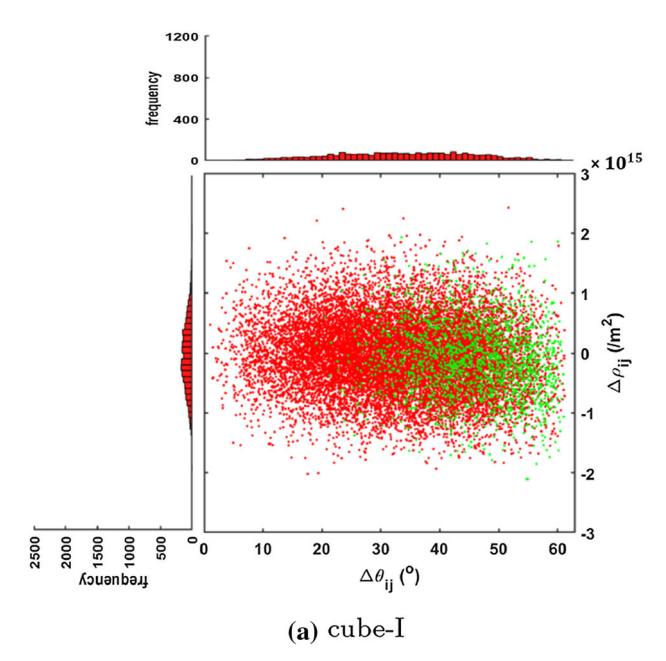
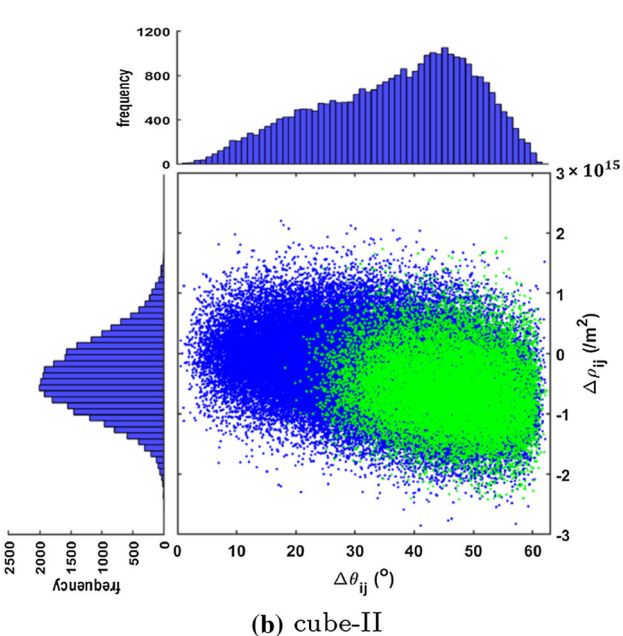


Fig. 12—A possible nucleation mechanism *via* strain induced boundary migration is shown schematically. HAB means high angle boundary and LAB means low angle boundary. Low stored energy regions are shown with larger cell size and lower misorientation angle (1 to 2 deg), whereas, high stored energy regions are shown with smaller cell size and higher misorientation angle (4 to 5 deg). With the start of the annealing process, larger cells start to invade the region of lower cell size and one of the larger cells grows large enough to get significant size advantage over other cells.





**◄** Fig. 13—Scatter plots for (*a*) cube-I and (*b*) cube-II showing dislocation density difference ( $\Delta \rho$ ) and corresponding disorientation angle ( $\Delta \theta$ ) with its six nearest neighbor material points in M1 at  $\epsilon_{vM}$  of 1.38. Green markers show the S-oriented neighbors in both (a) and (b). Histograms of  $\Delta \rho$  and  $\Delta \theta$  are also shown on the left and top of the scatter plots, respectively (Color figure online).

analyzed. For this purpose, different combinations of dislocation density difference and disorientation angle with the nearest neighbors were utilized. The main findings of this study are as follows:

- 1. Two types of the cube band were observed in the deformed microstructure, one which was retained in the initial cube grains (cube-I) and the other which was originated from the non-cube grains during the deformation (cube-II). With increasing deformation, both the cube-I and the cube-II got thinner and were mostly located near the intergranular region.
- 2. During early stages of deformation, the cube-II developed in the grains which were within 10 to 20 deg from the ideal cube orientation. However, with increasing strain, frequency of cube-II in these grains decreased and grains which were further away from the ideal cube orientation developed the cube-II. The axis distribution also evolved during the deformation and the distribution was different in two different microstructures. Hence, the possible grain orientations, in which the cube component can develop, will vary with the microstructure and level of deformation.
- 3. The cube component developed during deformation was unstable and rotated away from the cube orientation with further deformation. Hence, evolution of the cube-II becomes dynamic at larger strain, where the cube component developed earlier starts to rotate away from the cube orientation, while, other non-cube grains rotate towards the cube component.
- 4. Both the cube components had higher disorientation angles with their neighbors, hence, their relative volume fraction and  $\Delta \rho$  will play more important

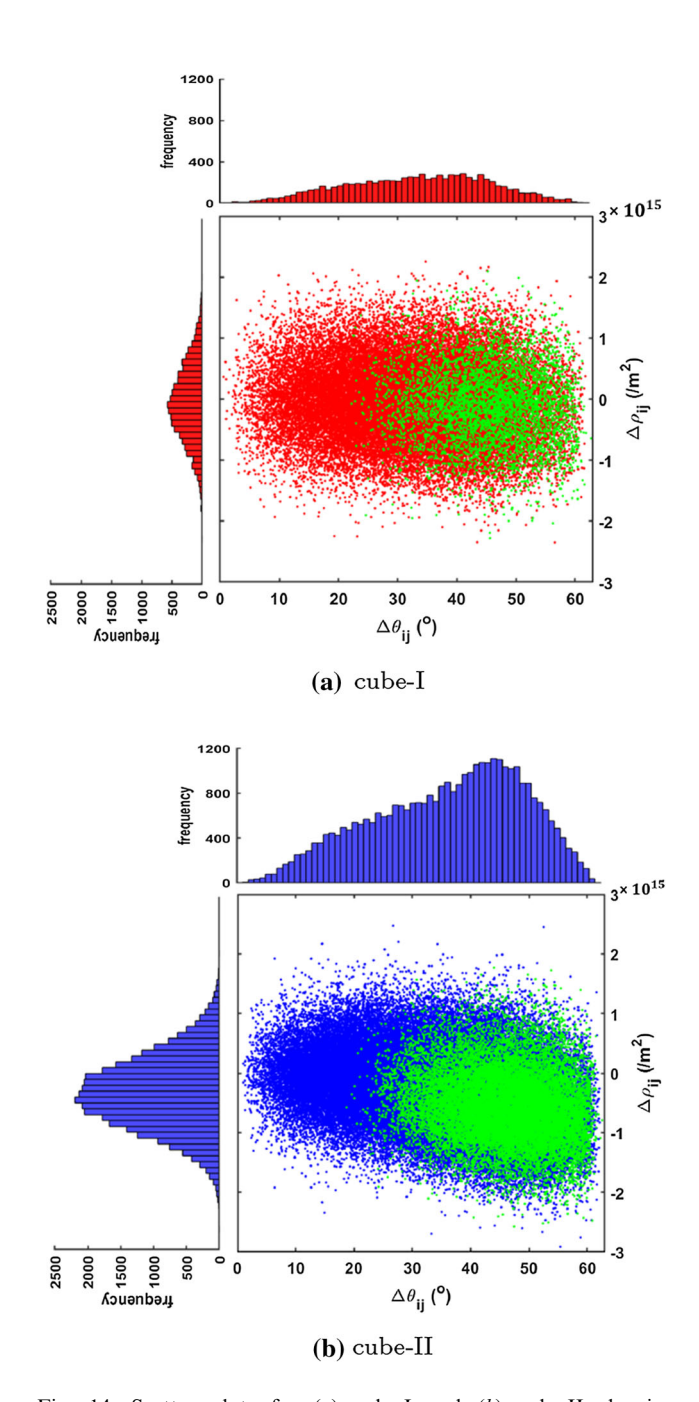
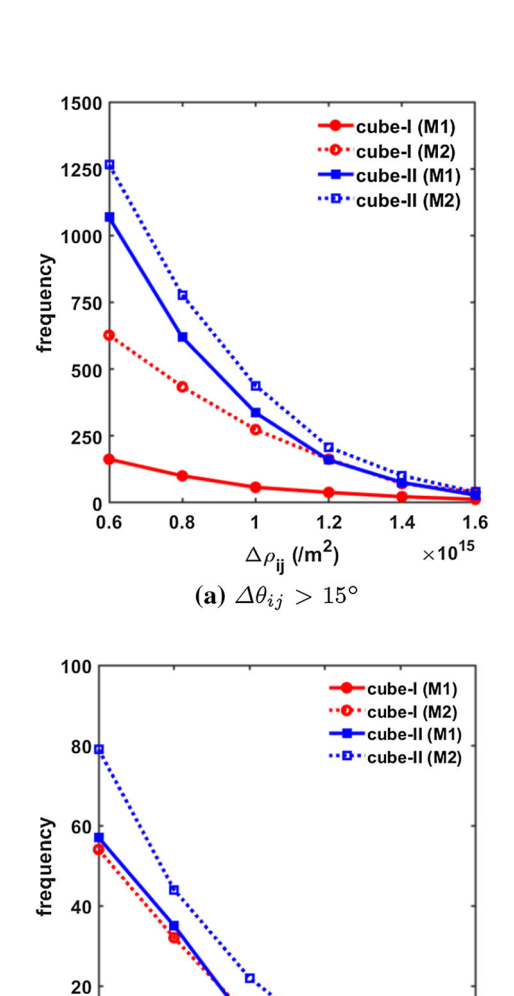


Fig. 14—Scatter plots for (a) cube-I and (b) cube-II showing dislocation density difference ( $\Delta \rho$ ) and corresponding disorientation angle ( $\Delta \theta$ ) with its six nearest neighbor material points in M2 at  $\epsilon_{vM}$  of 1.38. Green markers show the S-oriented neighbors in both (a) and (b). Histograms of  $\Delta \rho$  and  $\Delta \theta$  are also shown on the left and top of the scatter plots, respectively (Color figure online).

role in determining the nucleation propensity during recrystallization.

5. Irrespective of the nucleation condition, the cube-II shows significant propensity for nucleation of the cube-oriented recrystallized grains.



(b) S-oriented neighbor Fig. 15—Frequency of the cube-I and the cube-II is plotted with the variation of  $\Delta \rho_{ij}$  for two different nucleation conditions, (a) the relaxed condition with  $\Delta \theta_{ij} > 15$  deg and (b) the stringent condition with S-oriented neighbor. Results for both the RVE M1 and M2 are presented.

 $\Delta 
ho_{ij}$  (/m²)

0.6

0.8

## **ACKNOWLEDGMENTS**

The authors want to acknowledge the National Science Foundation, Division of Civil, Mechanical and Manufacturing Innovation for their support under the Grant No. CMMI-1662646. SC and CSP want to acknowledge the Simulation Innovation and Modeling Center, The Ohio State University and Ohio Supercomputer Center for providing computational resources. The authors also like to thank Prof. Anthony Rollett and Prof. Roger Doherty for valuable discussions.

1.6

 $\times 10^{15}\,$ 

The authors declare that they have no conflict of interest.

See Fig. A1, Tables A1 and A2.

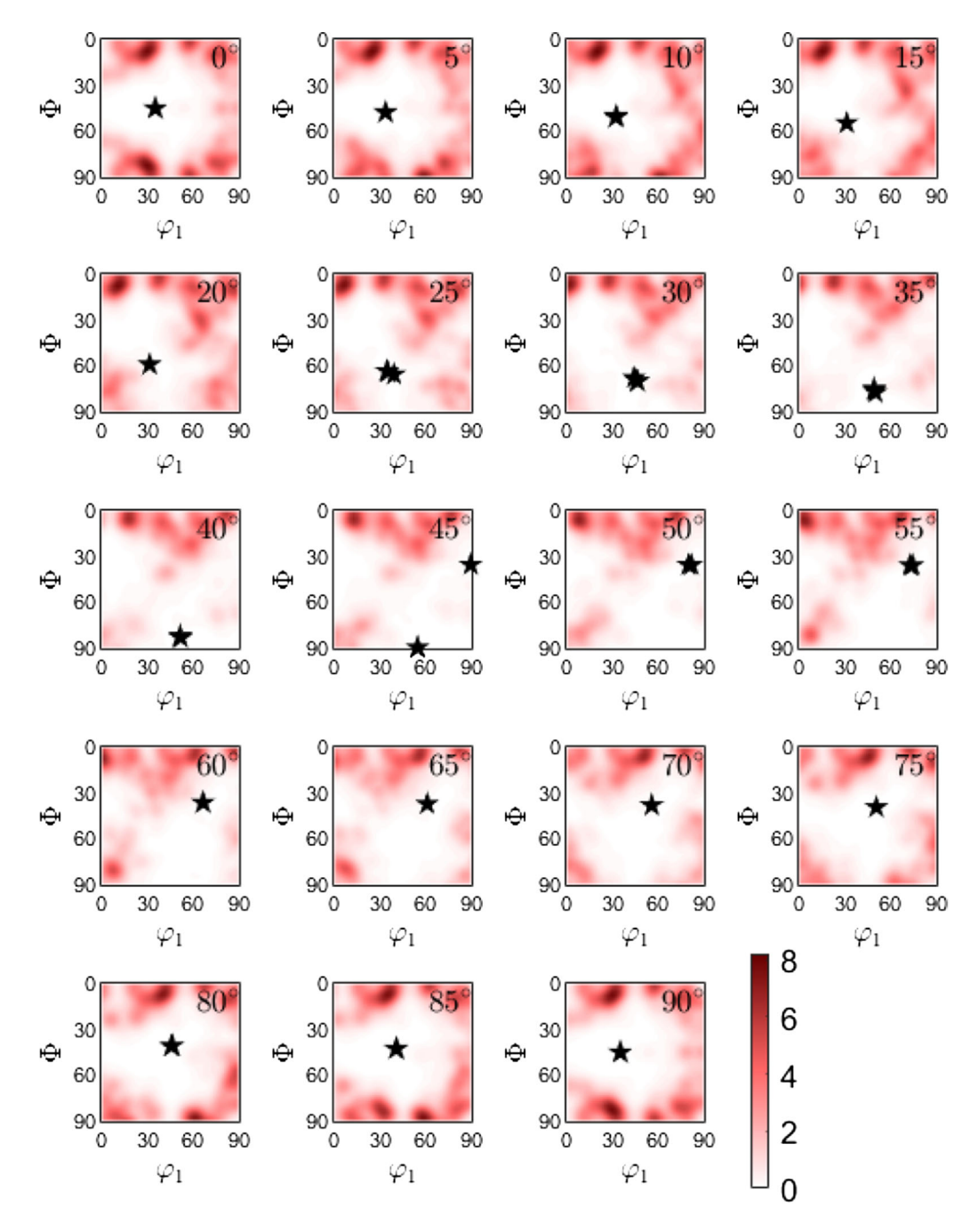


Fig. A1—ODF corresponding to the non-cube grains which developed the cube component at strain of  $\epsilon_{vM}=1.38$  in RVE M1, is presented in 2D sections of reduced Euler space. The  $\beta$ -fiber coordinates, as defined in the work of Sidor and Kestens, are also shown using star shaped markers. Very low intensity around the  $\beta$ -fiber is clearly visible.

Table A1. Miller Indices and Euler Angles of the Main Texture Components [65,70]

Texture Components	Miller Indices	Variants	Euler Angles (Bunge, $\phi_1, \Phi, \phi_2$ )
Cube	$\{100\}\langle001\rangle$	_	0 deg, 0 deg, 0 deg
Goss	$\{110\}\langle001\rangle$	_	0 deg, 45 deg, 0 deg
Copper	$\{112\}\langle 11\overline{1}\rangle$	CuI	90 deg, 35 deg, 45 deg
S	(122) / (24)	Cu <sub>II</sub> SI	270 deg, 35 deg, 45 deg
3	$\{123\}\left\langle 63\overline{4}\right\rangle$	$S_{\mathrm{II}}$	59 deg, 37 deg, 63 deg 239 deg, 37 deg, 63 deg
		$S_{III}$	301 deg, 143 deg, 243 deg
		$\mathrm{S}_{\mathrm{IV}}$	121 deg, 143 deg, 243 deg
Brass	$\{110\}\langle 1\bar{1}2\rangle$	$\mathrm{Br}_{\mathrm{I}}$	35 deg, 45 deg, 90 deg
	,	$\mathrm{Br}_{\mathrm{II}}$	325 deg, 135 deg, 270 deg

Table A2. Orientation of Grain G1, G2 and G3 and Their Corresponding Orientations in the Experiment

Orientation in Simulation (Angle–Axis Pair)	Orientation in Experiment <sup>[26]</sup> (Angle–Axis Pair)
G1 - 34.3 deg/(- 0.117,0.093,0.988)	27 deg/(0.0,0.0,1.0)
G2 - 31.8 deg/(0.115,0.9,0.42)	28 deg/(0.0,0.89,0.46)
G3 - 23.5 deg/(0.55,0.0726,0.83)	25 deg/(0.39,0.43,0.81)

## SUPPLEMENTARY INFORMATION

The online version contains supplementary material available at https://doi.org/10.1007/s11661-021-06513-0.

# REFERENCES

- 1. O. Engler and J. Hirsch: *Mater. Sci. Eng. A*, 2002, vol. 336 (1–2), p. 249
- H. Inoue and T. Takasugi: Mater. Trans., 2007, vol. 48 (8), p. 2014.
- J.J. Sidor, Q. Xie, P. Chakravarty, and G. Pal: *IOP Conf. Ser. Mater. Sci. Eng.*, 2021, vol. 1121, p. 012046.
- V.S. Sarma, J. Eickemeyer, A. Singh, L. Schultz, and B. Holzapfel: Acta Mater., 2003, vol. 51 (16), p. 4919.
- P.P. Bhattacharjee, R.K. Ray, and A. Upadhyaya: *J. Mater. Sci.*, 2007, vol. 42 (6), p. 1984.
- 6. Y.V. Khlebnikova, D. Rodionov, I. Gervas'eva, T. Suaridze, and V. Kazantsev: *Tech. Phys. Lett.*, 2015, vol. 41 (4), p. 341.
- A. Ridha and W. Hutchinson: Acta Metall., 1982, vol. 30 (10), p. 1929.
- 8. J. Hjelen, R. Ørsund, and E. Nes: *Acta Metall. Mater.*, 1991, vol. 39 (7), p. 1377.
- B. Duggan, K. Lücke, G. Köhlhoff, and C. Lee: *Acta Metall. Mater.*, 1993, vol. 41 (6), p. 1921.
- R.D. Doherty, L.C. Chen, and I. Samajdar: *Mater. Sci. Eng. A*, 1998, vol. 257 (1), p. 18.
- I. Samajdar, B. Verlinden, L. Rabet, and P. Van Houtte: *Mater. Sci. Eng. A*, 1999, vol. 266 (1–2), p. 146.
- 12. K. Lücke: Can. Metall. Q., 1974, vol. 13 (1), p. 261.
- 13. D.J. Jensen: Acta Metall. Mater., 1995, vol. 43 (11), p. 4117.
- 14. R.D. Doherty: Prog. Mater. Sci., 1997, vol. 42 (1-4), p. 39.
- 15. F.J. Humphreys and M. Hatherly: Recrystallization and Related Annealing Phenomena, Elsevier, Amsterdam, 2012.
- R. Doherty, D. Hughes, F. Humphreys, J.J. Jonas, D.J. Jensen, M. Kassner, W. King, T. McNelley, H. McQueen, and A. Rollett: *Mater. Sci. Eng. A*, 1997, vol. 238 (2), p. 219.

- M.H. Alvi, S. Cheong, J. Suni, H. Weiland, and A. Rollett: *Acta Mater.*, 2008, vol. 56 (13), p. 3098.
- 18. A. Akef and J. Driver: Mater. Sci. Eng. A, 1991, vol. 132, p. 245.
- Q. Liu, N. Hansen, C. Maurice, and J. Driver: *Metall. Mater. Trans. A*, 1998, vol. 29A (9), p. 2333.
- 20. I. Dillamore and H. Katoh: Metal Sci., 1974, vol. 8 (1), p. 73.
- 21. F. Basson and J. Driver: Acta Mater., 2000, vol. 48 (9), p. 2101.
- 22. J. Wert, Q. Liu, and N. Hansen: *Acta Mater.*, 1997, vol. 45 (6), p. 2565.
- T. Kamijo, A. Fujiwara, Y. Yoneda, and H. Fukutomi: *Acta Metall. Mater.*, 1991, vol. 39 (8), p. 1947.
- 24. T. Kamijo, H. Adachihara, and H. Fukutomi: *Acta Metall. Mater.*, 1993, vol. 41 (3), p. 975.
- R. Quey, P. Dawson, and J. Driver: J. Mech. Phys. Solids, 2012, vol. 60 (3), p. 509.
- A. Albou, R. Quey, C. Maurice, S. Raveendra, I. Samajdar, P.R. Dawson, and J.H. Driver: *Mater. Sci. Forum*, 2012, vol. 702, pp. 385–90.
- I. Samajdar and RD. Doherty: Scripta Metallurgica et Materialia, 1995, vol. 32, p. 6.
- S. Zaefferer, T. Baudin, and R. Penelle: *Acta Mater.*, 2001, vol. 49 (6), p. 1105.
- A. Albou, S. Raveendra, P. Karajagikar, I. Samajdar, C. Maurice, and J.H. Driver: Scripta Mater., 2010, vol. 62 (7), p. 469.
- O. Sukhopar and G. Gottstein: *Mater. Sci. Forum*, 2014, vol. 794, pp. 1245–1250.
- A. Beaudoin, Jr, H. Mecking, and U. Kocks: *Philos. Mag. A*, 1996, vol. 73 (6), p. 1503.
- J.J. Sidor, R.H. Petrov, and L.A. Kestens: Acta Mater., 2011, vol. 59 (14), p. 5735.
- K. Adam, D. Zöllner, and D.P. Field: *Modell. Simul. Mater. Sci. Eng.*, 2018, vol. 26 (3), art. no. 035011.
- 34. M. Zecevic, R.A. Lebensohn, R.J. McCabe, and M. Knezevic: *Acta Mater.*, 2019, vol. 164, p. 530.
- 35. G. Falkinger, P. Simon, and S. Mitsche: *Metall. Mater. Trans. A*, 2020, vol. 51A (6), p. 3066.
- C.S. Patil, S. Chakraborty, and S.R. Niezgoda: *Int. J. Plast.*, 2021, vol. 147, p. 103099.
- 37. R.A. Lebensohn, A.K. Kanjarla, and P. Eisenlohr: *Int. J. Plast.*, 2012, vol. 32, p. 59.
- 38. R.A. Lebensohn, R. Brenner, O. Castelnau, and A.D. Rollett: *Acta Mater.*, 2008, vol. 56 (15), p. 3914.

- 39. M. Diehl, D. An, P. Shanthraj, S. Zaefferer, F. Roters, and D. Raabe: *Phys. Mesomech.*, 2017, vol. 20 (3), p. 311.
- C. Slone, S. Chakraborty, J. Miao, E.P. George, M.J. Mills, and S. Niezgoda: *Acta Mater.*, 2018, vol. 158, p. 38.
- 41. F. Roters, M. Diehl, P. Shanthraj, P. Eisenlohr, C. Reuber, S.L. Wong, T. Maiti, A. Ebrahimi, T. Hochrainer, H.O. Fabritius *et al.: Comput. Mater. Sci.*, 2019, vol. 158, p. 420.
- 42. R.A. Lebensohn and A.D. Rollett: *Comput. Mater. Sci.*, 2020, vol. 173, p. 109336.
- 43. E. Orowan: Z. Phys., 1934, vol. 89 (9-10), p. 605.
- 44. H. Conrad: JOM, 1964, vol. 16 (7), p. 582.
- 45. U.F. Kocks, A. AS, A. MF, (1975).
- 46. A. Ma and F. Roters: Acta Mater., 2004, vol. 52 (12), p. 3603.
- A. Ma, F. Roters, and D. Raabe: *Acta Mater.*, 2006, vol. 54 (8), p. 2169.
- 48. M. Ashby: Philos. Mag., 1970, vol. 21 (170), p. 399.
- 49. P. Jackson and Z. Basinski: Can. J. Phys., 1967, vol. 45 (2), p. 707.
- P. Franciosi, M. Berveiller, and A. Zaoui: *Acta Metall.*, 1980, vol. 28 (3), p. 273.
- 51. Z. Basinski: Discuss. Faraday Soc., 1964, vol. 38, p. 93.
- B. Devincre, L. Kubin, and T. Hoc: Scripta Mater., 2007, vol. 57 (10), p. 905.
- 53. T. Ohashi: Philos. Mag., 2018, vol. 98 (25), p. 2275.
- T. Hochrainer and B. Weger: *J. Mech. Phys. Solids*, 2020, vol. 141, p. 103957.
- 55. R. Balluffi: *Physica Status Solidi* (b), 1970, vol. 42 (1), p. 11.
- 56. A. Cuitino and M. Ortiz: Acta Mater., 1996, vol. 44 (2), p. 427.
- 57. P.M. Anderson, J.P. Hirth, and J. Lothe: *Theory of Dislocations*, Cambridge University Press, Cambridge, 2017.
- 58. C. Kords, On the role of dislocation transport in the constitutive description of crystal plasticity. Ph.D. thesis (2013).
- R.W. Balluffi, S.M. Allen, and W.C. Carter: Kinetics of Materials, Wiley, Hoboken, 2005.
- H. Bowden and R. Balluffi: *Philos. Magn.*, 1969, vol. 19 (161), p. 1001.
- 61. E. Oren and C.L. Bauer: Acta Metall., 1967, vol. 15 (5), p. 773.
- 62. M. Wuttig and H. Birnbaum: Phys. Rev., 1966, vol. 147 (2), p. 495.
- 63. M.A. Groeber and M.A. Jackson: *Integr. Mater. Manuf. Innov.*, 2014, vol. 3 (1), p. 56.
- 64. F.X. Lin, W. Pantleon, T. Leffers, and D.J. Jensen: *Mater. Sci. Forum*, 2012, vol. 702, pp. 398–401.
- F. Lin: Recrystallization of Deformed Copper: Kinetics and Microstructural Evolution, Technical University of Denmark, Lyngby, 2013.

- C.A. Bronkhorst, Plastic deformation and crystallographic texture evolution in face-centered cubic metals. Ph.D. thesis, Massachusetts Institute of Technology (1991).
- 67. W. Overton, Jr and J. Gaffney: *Phys. Rev.*, 1955, vol. 98 (4), p. 969.
- H. Ledbetter and E. Naimon: J. Phys. Chem. Ref. Data, 1974, vol. 3 (4), p. 897.
- 69. F. Bachmann, R. Hielscher, and H. Schaeben: *Solid State Phenomena*, 2010, vol. 160, pp. 63–68.
- U.F. Kocks, C.N. Tomé, and H.R. Wenk: Texture and Anisotropy: Preferred Orientations in Polycrystals and Their Effect on Materials Properties, Cambridge University Press, Cambridge, 1998.
- 71. T. Leffers and R. Ray: Prog. Mater. Sci., 2009, vol. 54 (3), p. 351.
- 72. N. Gurao, S. Sethuraman, and S. Suwas: *Mater. Sci. Eng. A*, 2011, vol. 528 (25–26), p. 7739.
- 73. J. Vallin, M. Mongy, K. Salama, and O. Beckman: *J. Appl. Phys.*, 1964, vol. 35 (6), p. 1825.
- C. Maurice and J. Driver: *Acta Metall. Mater.*, 1993, vol. 41 (6), p. 1653.
- 75. C. Maurice and J. Driver: *Acta Mater.*, 1997, vol. 45 (11), p. 4627.
- J.J. Sidor and L.A. Kestens: Scripta Mater., 2013, vol. 68 (5), p. 273.
- 77. O. Engler and V. Randle: *Introduction to Texture Analysis: Macrotexture, Microtexture, and Orientation Mapping*, CRC Press, Boca Raton, 2009.
- 78. P.R. Rios, F. Siciliano, Jr., H.R.Z. Sandim, R.L. Plaut, and A.F. Padilha: *Mater. Res.*, 2005, vol. 8 (3), p. 225.
- 79. P.A. Beck and P.R. Sperry: *J. Appl. Phys.*, 1950, vol. 21 (2), p. 150.
- 80. F. Humphreys: Acta Mater., 1997, vol. 45 (10), p. 4231.
- E.A. Holm, M.A. Miodownik, and A.D. Rollett: *Acta Mater.*, 2003, vol. 51 (9), p. 2701.
- 82. V.M. Miller, A.E. Johnson, C.J. Torbet, and T.M. Pollock: *Metall. Mater. Trans. A*, 2016, vol. 47A (4), p. 1566.
- K. Traka, K. Sedighiani, C. Bos, J.G. Lopez, K. Angenendt, D. Raabe, and J. Sietsma: *Comput. Mater. Sci.*, 2021, vol. 198, p. 110643.
- 84. O. Engler: Mater. Sci. Technol., 1996, vol. 12 (10), p. 859.
- 85. A. Després, M. Greenwood, and C. Sinclair: Acta Mater., 2020, vol. 199, p. 116.
- 86. R. Quey, G.H. Fan, Y. Zhang, and D.J. Jensen: *Acta Mater.*, 2021, vol. 210, p. 116808.

**Publisher's Note** Springer Nature remains neutral with regard to jurisdictional claims in published maps and institutional affiliations.